

# Effect of Annealing on the Microstructure, Texture and Mechanical Properties of a Dual-Phase Ultrahigh-strength TWIP Steel



N.K. TEWARY, S.K. GHOSH, A. MANDAL, D. CHAKRABARTI,  
and S. CHATTERJEE

The present study investigates the effect of annealing time and temperature on the microstructural restoration (by recovery and recrystallization), texture evolution and tensile properties of a dual-phase TWIP steel. The samples, which were initially hot rolled-air cooled followed by being in solution treated condition, subsequent 50 pct cold rolled condition and different annealing conditions (temperatures ranging from 500 °C to 1000 °C for 5 minutes to 2 hours), were subjected to microstructural characterization using optical and transmission electron microscopy, electron backscatter diffraction analysis, tensile testing and fractographic study. The deformation-induced ferrite (DIF) transformation due to cold deformation, the evolution of the grain structure and texture in both austenite and ferrite, and the change in the DIF fraction (accompanying the recrystallization annealing treatment) are critically analyzed. The optimum combination of strength and ductility is achieved in the partially recrystallized samples annealed at 700 °C for 30 minutes (UTS: 859 MPa, total elongation: 37 pct) and 900 °C for 30 minutes (UTS: 708 MPa, total elongation: 63 pct). The effects of DIF on the evolution of microstructure and texture during annealing and the final properties are discussed.

<https://doi.org/10.1007/s11661-020-05851-9>

© The Minerals, Metals & Materials Society and ASM International 2020

## I. INTRODUCTION

THE research interest in low-carbon, high-manganese twinning-induced plasticity (TWIP) steels has continuously increased because of their attractive strength-ductility combination along with excellent work-hardening capacity.<sup>[1]</sup> Addition of lighter elements such as Al reduces the density of TWIP steel, which helps in lowering the vehicle weight and decreasing the associated CO<sub>2</sub> emission and environmental pollution.<sup>[2]</sup> The high Mn content makes the austenite stable at room temperature and maintains the stacking fault energy (SFE) in the range of 20 to 40 mJ/m<sup>2</sup>.<sup>[3]</sup> As a result, the primary deformation mechanism produces twinning instead of deformation by a slip or martensitic transformation.<sup>[4]</sup> Martensitic transformation can always be accompanied by twinning. Al addition increases the SFE<sup>[5]</sup> and corrosion resistance<sup>[6]</sup> and prevents delayed

fracture during the tensile deformation of TWIP steel.<sup>[7]</sup> Addition of Si in TWIP steel helps to avoid carbide precipitation.<sup>[8]</sup> A small amount of Si addition mainly at lower temperatures retards cementite precipitation in austenite by the reduction of the free energy change of the Fe<sub>3</sub>C reaction, which slows down the kinetics of precipitation.<sup>[9–11]</sup> The presence of low carbon in this steel provides excellent weldability and formability and avoids undesirable carbide formation.<sup>[12]</sup> Recent research on the dual-phase TWIP steel is designed so that part of the austenite is deformed by the twinning mechanism during straining, while the remaining austenite undergoes deformation-induced transformation to a harder ferrite phase.<sup>[13–17]</sup> As a result, higher tensile strength can be achieved along with high ductility. The development of ferrite-austenite dual-phase TWIP steel requires a controlled addition of alloying elements, especially Al.

Earlier studies established a combined deformation mechanism involving twinning and dislocation movement in TWIP steel. As a result, high strength can be achieved along with a high strain-hardening ability that ensures high uniform elongation.<sup>[13–17]</sup> In the present study, the carbon content was kept as low as 0.06 wt pct to reduce the chances of carbide formation. The composition was selected to get a dual-phase structure of ferrite and austenite as low-carbon dual-phase TWIP

---

N.K. TEWARY, S.K. GHOSH, and S. CHATTERJEE are with the Department of Metallurgy & Materials Engineering, Indian Institute of Engineering Science and Technology, Shibpur, Howrah 711103, India. Contact e-mail: skghosh@metal.iiests.ac.in A. MANDAL and D. CHAKRABARTI are with the Department of Metallurgical and Materials Engineering, Indian Institute of Technology, Kharagpur, Kharagpur 721302, India.

Manuscript submitted June 22, 2019.

Article published online June 18, 2020

steel<sup>[18]</sup> has the better combination of strength and ductility compared with that of (strain induced martensite + austenite) TWIP/TRIP steel.<sup>[19]</sup>

During cold rolling, the deformation twins decrease the mean free path of dislocation movement resulting in dislocation-twin interaction that, along with the twin-twin interaction, significantly increases the tensile strength. A detailed investigation of the microstructural restoration during the recrystallization annealing treatment is necessary to achieve the best possible combination of strength and ductility in TWIP steel. The annealing response of TWIP steel follows successive stages of recovery, partial and complete recrystallization and grain growth. Some of the earlier studies investigated the annealing response of cold-deformed samples of different grades of TWIP steels having a composition range of 17 to 24 Mn, 1.5 to 3.0 Al, 0.0 to 2.0 Si, 0 to 1 Ni, 0.06 to 0.30 C and the rest iron (all in wt pct).<sup>[20–23]</sup> Annealing treatments were carried out at 300 °C to 900 °C (especially at 600 °C to 700 °C) for 60 minutes.<sup>[20–23]</sup> However, consistent and in-depth understanding of the effect of annealing treatment on the recovery and recrystallization mechanism is yet to be achieved. Regarding the deformation mechanism of dual-phase ferrite-austenite TWIP steel, the previous studies were primarily focused on the hot and cold deformation behavior instead of the annealing response. Mohamadizadeh *et al.*<sup>[24]</sup> performed electron backscatter diffraction (EBSD) analysis on a hot, deformed (at 1000 °C using 1/s strain-rate) duplex low-density steel (0.7 C-17 Mn-8 Al) and reported the formation of ultrafine ferrite grains (~ 0.3 μm diameter) by deformation-induced austenite to ferrite transformation. The presence of alpha fibers such as Brass and Goss texture components are expected in low SFE TWIP steel.<sup>[25]</sup> During deformation, the intensity of the Cu component is reduced while that of the Brass component is increased.<sup>[26]</sup> Also, the deformation texture intensity decreases upon annealing.<sup>[27]</sup> However, the influence of deformation-induced ferrite transformation on texture formation has not been discussed so far. In addition, the evolution of microstructure and crystallographic texture in the cold-rolling and annealing route and the associated changes in tensile properties have not been investigated for the current dual-phase TWIP steel.

Therefore, the present investigation aims to study the effect of annealing time and temperature on the microstructural restoration (by recovery and recrystallization) as well as texture evolution and the tensile properties of a dual-phase TWIP steel.

## II. EXPERIMENTAL PROCEDURES

The chemical composition of the investigated steel is shown in Table I. The steel was prepared in an air induction furnace, and the final ingot size was 200 mm × 100 mm × 100 mm after discarding the shrinkage portion. The ingot was homogenized at 1200 °C for 5 hours and subsequently hot forged to a long bar with a cross-section area of 18 mm × 24 mm. Small pieces were cut from the forged bar with a size of 60 mm × 18 mm ×

**Table I. Nominal Chemical Composition (Weight Percent) of the Investigated Dual-Phase TWIP Steel**

C	Mn	Si	Al	S	P	Fe
0.06	21.50	3.11	3.56	0.009	0.008	balance

24 mm and were soaked at 1200 °C for 40 minutes for hot rolling. The finish rolling temperature (FRT) was 800 °C, and the samples were air cooled from FRT to room temperature. The final thickness of the hot-rolled plate was 8 mm (reduced from 18 mm). A solution treatment (at 1040 °C for 1 hour) followed by water quenching was adopted to remove the inhomogeneities in the hot-rolled samples. The hot-rolled, air-cooled and solution-treated (HRACST) samples were cold rolled at room temperature to 50 pct thickness reduction by applying several passes using a laboratory rolling mill. Finally, 50 pct cold-deformed samples were annealed at 500 °C, 600 °C, 700 °C, 800 °C, 900 °C and 1000 °C for different durations (5, 15, 30 minutes, 1 and 2 hours) followed by water quenching.

The Vickers hardness (HV) was examined using a Universal Hardness Tester (Innovatest VERZUS 750 series), applying 30 kgf force for 20 seconds of dwelling time. Dog-bone-shaped tensile specimens (ASTM E8M standard) were prepared with a gauge length of 25 mm, width of 6.35 mm and thickness of 3.1 mm. The tensile specimens were machined from the plates processed at different conditions (hot rolled, cold rolled or annealed) along the rolling direction. The tensile test was carried out at room temperature using an Instron 5900R machine at a crosshead velocity of 0.5 mm per minute. The strain was measured by a calibrated extensometer. The average hardness (ten readings from each specimen) and tensile strength were determined after testing a minimum of three specimens for each processing condition. The tensile toughness is the energy absorption capacity, which has been measured from the area of the plastic region of the stress-strain curve. The tensile toughness was calculated considering the yield and ultimate tensile strength along with ductility (tensile strain). For estimation of the recrystallized fraction (pct), the following equation<sup>[22,28]</sup> was used:

$$\text{Recrystallization (pct)} = \frac{HV_{CD} - HV_{ANN}}{HV_{CD} - HV_{INT}} \quad [1]$$

where  $HV_{CD}$ ,  $HV_{ANN}$  and  $HV_{INT}$  are the hardness values of cold-deformed, annealed and initial ‘undeformed condition,’ respectively.

For the microstructural study, the conventional metallographic procedure was followed, and the specimens were etched with 10 pct nital solution. Microstructural characterization was performed using a Carl Zeiss AXIOVERT 40 MAT optical microscope. The average austenite grain size was determined by measuring the area of > 500 grains from each sample and represented as the equivalent circle diameter. The 3-mm-diameter circular discs were punched out from thin foils (≈ 80

$\mu\text{m}$ ) and electro-polished (at  $\sim 10^\circ\text{C}$ ) using an electrolyte of 90 pct acetic acid and 10 pct perchloric acid. The transmission electron microscopy (TEM) study was performed in Tecnai@G<sup>2</sup> at 200 kV operating voltage. The phases present after the different processes were examined by an X-ray diffraction machine (Bruker-Advance D8 model) using a copper target ( $\text{CuK}\alpha$ ) at a step size of 0.01 deg/s and scanning over  $2\theta$  range of 40 to 100 deg. The specimens for electron backscatter diffraction (EBSD) study were prepared by mechanical polishing followed by electro-polishing in perchloric acid (5 vol pct) and acetic acid (95 vol pct) solutions. EBSD study was conducted in a Zeiss EVO 60 SEM with an attached Oxford HKL Channel 5 system. The 0.4- $\mu\text{m}$  step size was used to construct the EBSD maps on the 80  $\mu\text{m} \times 60 \mu\text{m}$  scan area. A minimum misorientation threshold of 2 deg was selected considering the angular resolution of EBSD. The boundaries having misorientation angles of 2 to 15 deg and  $> 15$  deg were considered the low- and high-angle boundaries, respectively.

### III. RESULTS AND DISCUSSION

#### A. Phase Identification from X-ray Diffraction

The X-ray diffraction peaks for the hot-rolled solution-treated (HRACST) and 50 pct cold (rolled) deformed (50CD) samples in Figure 1 show primarily austenite ( $\gamma$ -FCC) and ferrite ( $\alpha$ -BCC). The peak broadening due to cold deformation is evident in the 50CD sample (Figure 1). The (111), (200), (220), (311) and (222) peaks are identified for austenite.<sup>[29]</sup> On the other hand, the ferrite phase is recognized by the presence of (110), (200), (211) and (220) peaks. This ferrite is the deformation-induced ferrite (DIF), which contains a  $\text{DO}_3$  (example  $\text{Fe}_3\text{Al}$ ) type intermetallic precipitate.<sup>[24]</sup> However, the  $\text{Fe}_3\text{Al}$  ( $\text{DO}_3$ ) phase could not be detected in the present XRD study, possibly because of its low volume fraction, which is in agreement with an earlier study.<sup>[30]</sup>

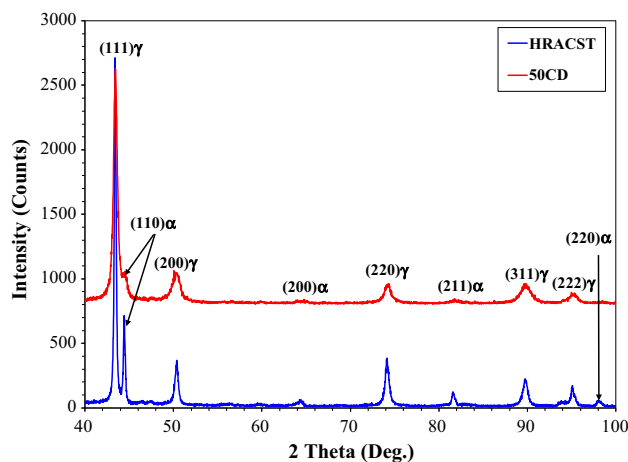


Fig. 1—X-ray diffraction profiles of hot rolled-solution annealed (HRACST) and 50 pct cold deformed (50CD) samples.

#### B. Microstructure Evolution

Figures 2(a) through (h) show the optical micrographs of HRACST, 50CD and annealed samples. The HRACST microstructure reveals equiaxed austenite grains containing the annealing twins and DIF along the grain boundaries. The 50CD sample shows DIF and some deformation twins within the austenite grains. A similar observation of DIF by optical microscopy has been reported earlier.<sup>[31]</sup>

Twinning is known to dominate the deformation mechanism in materials having SFE in the range of 20 to 40  $\text{mJ}/\text{m}^2$  such as TWIP steel. DIF generally evolves during and after hot rolling<sup>[32]</sup> as the austenite-to-ferrite transformation temperature increases with the increase in applied strain.<sup>[33]</sup> The DIF transformation involves diffusion of carbon and Mn into the austenite and Si and Al into the ferrite. The DIF transformation is also accompanied by stress relaxation. Al and Si are ferrite stabilizers and promote the ferrite transformation. Considering the cumulative effect of carbon and Mn, the low carbon content (0.06 wt pct) of the investigated steel reduces the stability of austenite. Carbon diffuses from the  $\alpha/\gamma$  interface to nearby austenite and forms DIF along the austenite grain boundaries. The ferrite nucleates during hot rolling and during subsequent slow cooling (air cooling); the strain relaxation causes the growth of the existing DIF. As the ferrite transformation depends not only on the thermal activation, but also on the applied strain, the ferrite is termed DIF.<sup>[34]</sup> These DIFs normally form during hot deformation/rolling and quenching in low-carbon steels.

However, as the hot-rolled sample is solution treated, the DIF disappears by the reverse ferrite-to-austenite transformation. An increase in the ferrite volume fraction during cold rolling can be related to the negative Helmholtz free energy as discussed below:

The Helmholtz energy,  $F$ , is defined as<sup>[35]</sup>

$$F = U - TS \quad [2]$$

where  $U$  is the internal energy of the system,  $T$  is the absolute temperature in Kelvin, and  $S$  is the entropy.

Again, from the first law of thermodynamics,<sup>[36]</sup>

$$dU = \delta Q - \delta W \quad [3]$$

where  $\delta Q$  is the energy of heating as expressed below and  $\delta W$  is the work done by the system:

$$\delta Q = TdS \quad [4]$$

As the cold rolling was performed at room temperature, the energy of heating will be negligible; therefore, the internal energy can be written as

$$dU = \delta Q - \delta W \quad [5]$$

The Helmholtz free energy becomes negative because of the total strain energy reduction induced by the cold work. Hence, there will be an enhancement of DIF formation since this contributes to a negative change in the Helmholtz free energy. As the specific volume of the



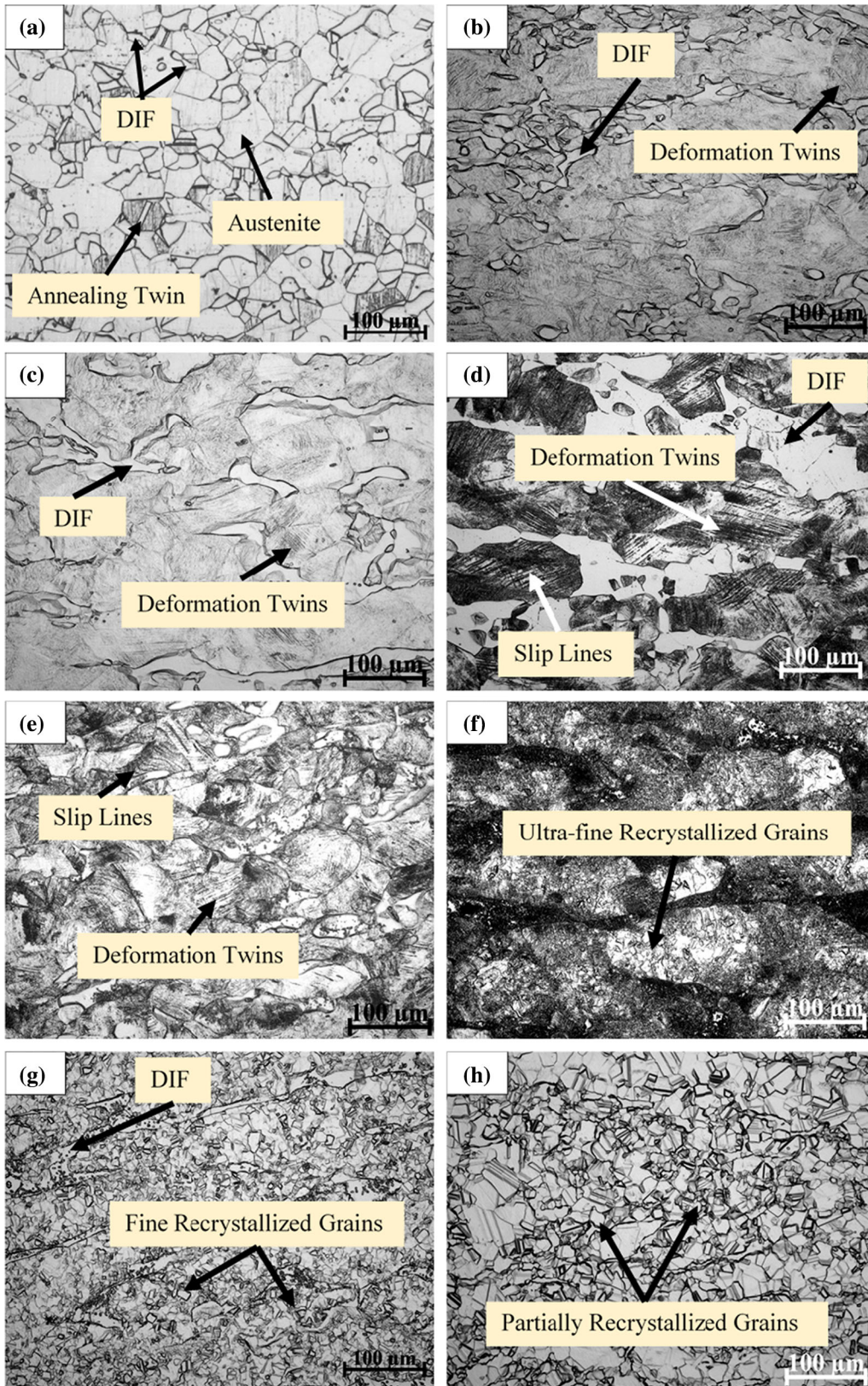


Fig. 2—Optical micrographs of (a) HRACST, (b) 50CD and annealed (c) 500 °C—5 min, (d) 500 °C—1 h, (e) 700 °C—5 min, (f) 700 °C—1 h, (g) 900 °C—5 min and (h) 900 °C—1 h samples.

DIF is less than that of the parent phase (matrix), the fraction of DIF increases because of the relaxation of the total strain energy (generated by the cold working), thereby reducing the total Helmholtz free energy of the system. The driving force,  $\Delta G_{xy}$ , for the deformation induced austenite-to-ferrite transformation, can be expressed as<sup>[37]</sup>

$$\Delta G_{xy} = \Delta G_{\text{chem}} + \Delta G_{\text{def}} \quad [6]$$

where  $\Delta G_{\text{chem}}$  is the chemical free energy, and  $\Delta G_{\text{def}}$  is the strain energy stored during deformation, which provides a supplementary driving force. The driving force ( $\Delta G_{xy}$ ) increases with the increase in applied strain, promoting the austenite-to-ferrite transformation. The Helmholtz free energy and driving force arising from the stored energy during deformation for the DIF transformation are given here to explain the enhancement in the volume percentage of the DIF according to the available literature.<sup>[35,37]</sup> However, no analysis of the above specific material parameter is done in the present study.

The DIF volume fraction depends on the carbon diffusion in austenite and the austenite/ferrite interface mobility. During the transformation, the mobility of the austenite/ferrite interface accumulates the carbon atoms into the surrounding austenite because of the lower solubility of carbon in ferrite.<sup>[38]</sup> At the time of hot rolling, the occurrence of dynamic recrystallization increases the grain boundaries of austenite. The DIF forms along those boundaries as they are high-energy regions. The accumulation of strain (*i.e.*, strain energy) during hot rolling intensifies the diffusion of alloying elements (through pipe diffusion) and provides the driving force for the DIF transformation.<sup>[39,40]</sup>

During cold rolling, the defects generated by deformation act as the preferred nucleation sites for ferrite formation through structure-sensitive diffusion. The carbon atoms diffuse during cold rolling by dislocation-assisted pipe diffusion<sup>[41]</sup> near the austenite/ferrite interfaces. The carbon atoms move following the concentration gradient in austenite. The austenite regions with lower carbon content become unstable, and the DIF transformation occurs.<sup>[41]</sup> Due to this strain-induced transformation, the ferrite contains high dislocation density. The DIF is harder than the normal ferrite as it contains a DO<sub>3</sub>-type phase of Fe<sub>3</sub>Al.<sup>[42]</sup> Optical micrographs of cold-rolled and annealed samples (at 500 °C for 5 minutes to 1 hour) in Figures 2(c) and (d) indicate no evidence of recrystallization. The presence of deformation twins after annealing at 500 °C suggests the occurrence only of recovery without any recrystallization. In this context, it is important to note that the microstructure remains unchanged even after annealing at 700 °C for 5 minutes (Figure 2(e)).

The recrystallized ultrafine austenite grains (~ 5 to 7 μm) are observed in certain regions (~ 20 vol pct) after annealing at 700 °C for 1 hour (Figure 2(f)). The recrystallized grains gradually become more prominent with increasing temperature and time of annealing. Annealing at 900 °C for 5 minutes reveals a partially recrystallized grain structure with some deformed grains (< 20 vol pct) as shown in Figure 2(g). Figure 2(h)

shows fine (~ 2 to 10 μm) and equiaxed recrystallized grains after annealing at 900 °C for 1 hour. Although the grains with defects and without defects can be difficult to distinguish in optical micrographs, fine and equiaxed grains are considered the recrystallized grains. To study the recrystallization phenomenon in TWIP steel, optical microscopy is preferred over other techniques.<sup>[24,25]</sup> Optical microscopy can cover a large sample area, which is beneficial and cannot be examined at higher magnification electron microscopy.

The TEM micrographs of HRACST, 50CD and annealed samples (at 500 °C and 900 °C for 30 minutes) are provided in Figure 3. The fully austenitic structure, along with annealing twins, is evident in the HRACST sample shown in Figure 3(a). Deformation twins within the austenite grains are observed in the 50 pct cold-deformed (50CD) sample shown in Figure 3(b). The inset of Figure 3(b) shows a selected area electron diffraction (SAED) pattern (taken from the circular region indicated in the micrograph), which confirms the presence of twins. It is important to note that the deformation twins (width: 40 to 50 nm) are much finer than the annealing twins (width: 150 to 170 nm) (Figure 3(a) *vis-à-vis* Figure 3(b)). Figure 3(c) shows the TEM bright-field (BF) micrograph of the 50CD sample where the deformation-induced ferrite (DIF) can be identified along the austenite grain boundary. As reported earlier,<sup>[43]</sup> these ferrites generally contain Fe<sub>3</sub>Al intermetallic precipitates having a superlattice structure (DO<sub>3</sub>). However, due to the small fraction of Fe<sub>3</sub>Al, these particles are difficult to detect. In this regard, to provide confirmation of the existence of the DO<sub>3</sub> in the ferrite phase, SAED (inset in Figure 3(c)) taken from the circular area is marked in the DIF grain. Imandoust *et al.*<sup>[44]</sup> presented a similar DO<sub>3</sub> phase (confirmed by SAED analysis) in the ferrite phase of a dual-phase TWIP steel [Fe-29.20Mn-5.20Al-0.60Si-0.06C (wt pct)] through TEM studies. Welsch *et al.*<sup>[45]</sup> showed a similar superlattice reflection in the diffraction pattern of a high Mn lightweight steel.

For the ordered structure, superlattice reflections are expected to be present. The actual real-space unit cell becomes larger because of the extra lattice points; thus, the reciprocal-space cell becomes smaller.<sup>[44,45]</sup> The intensity of this superlattice structure is lower than that of the fundamental lattice<sup>[45]</sup> and therefore appears to be very faint.<sup>[46]</sup> The presence of the deformation twin bundles at 500 °C for the 30-min annealed sample can be confirmed by the bright-field TEM image (Figure 3(d)). Annealing at 900 °C for 30 minutes shows recovered grains with deformation twins (Figure 3(e)). The coexistence of deformed regions containing some dislocations and deformation twins beside the recrystallized grains at 900 °C for the 30-minute annealed sample is shown in Figure 3(f).

### C. Study of Microstructure and Microtexture by EBSD

Figures 4(a) through (e) display the ND-inverse pole figure (IPF) maps of FCC austenite for HRACST, 50CD and annealed (at 500°C, 700°C and 900°C for 30 minutes) samples. The IPF maps represent the



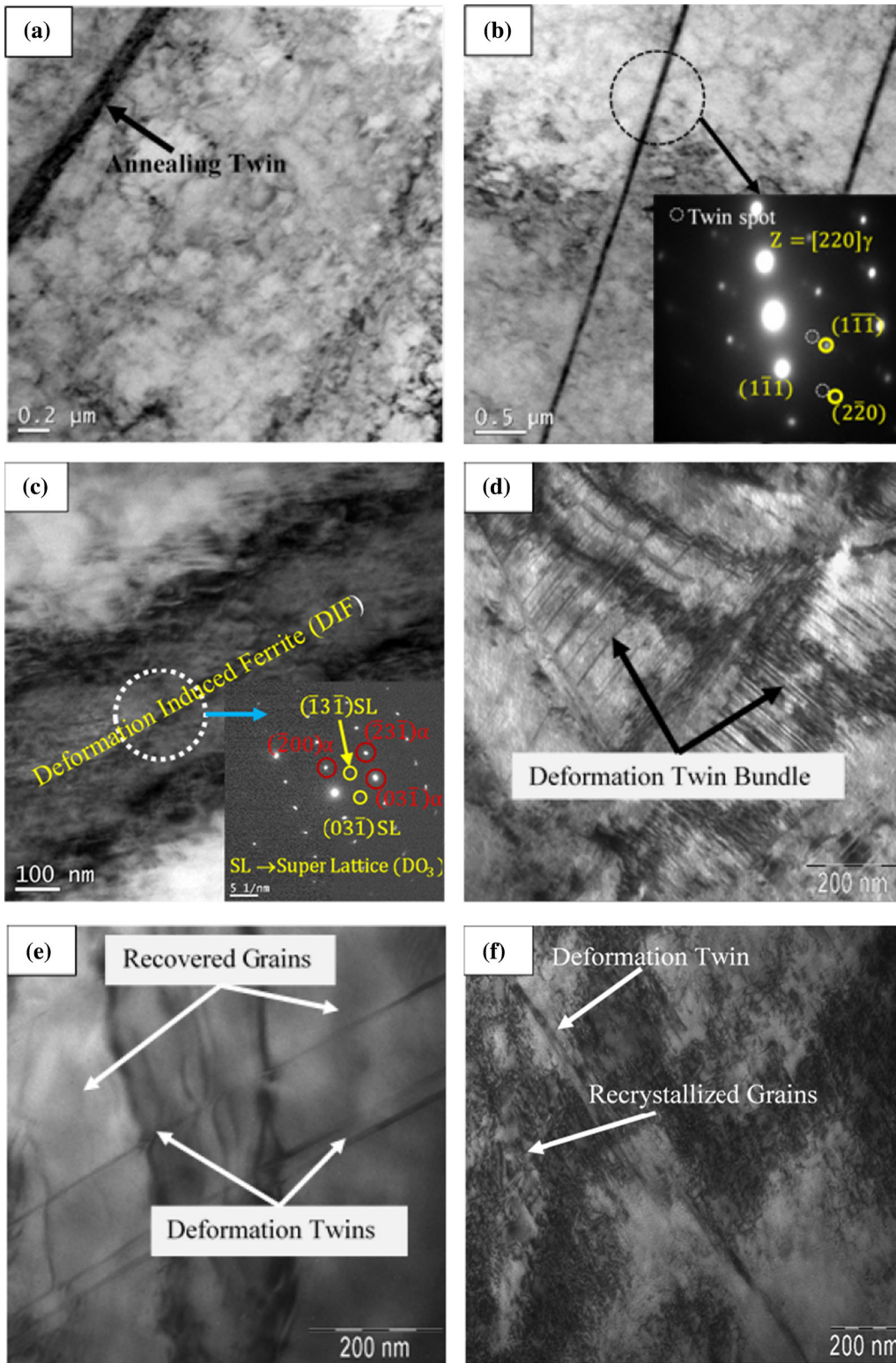


Fig. 3—TEM micrographs of (a) HRCST, (b and c) 50CD and annealed, (d) 500 °C—30 min, (e and f) 900 °C—30 min samples. Insets of (b) and (c) show the SAED patterns of the circular areas marked in the figures.

distribution of different orientations within the microstructure. Insets in Figures 4(a) through (e) are the twin maps of the respective IPF images. Figure 4(f) represents the ND-IPF color legend. The nucleation of

the recrystallized austenite grains, especially at the grain boundaries and the triple points, can be observed in the EBSD-IPF map in Figure 4(d). The austenite grain size in the partially recrystallized samples shows a large

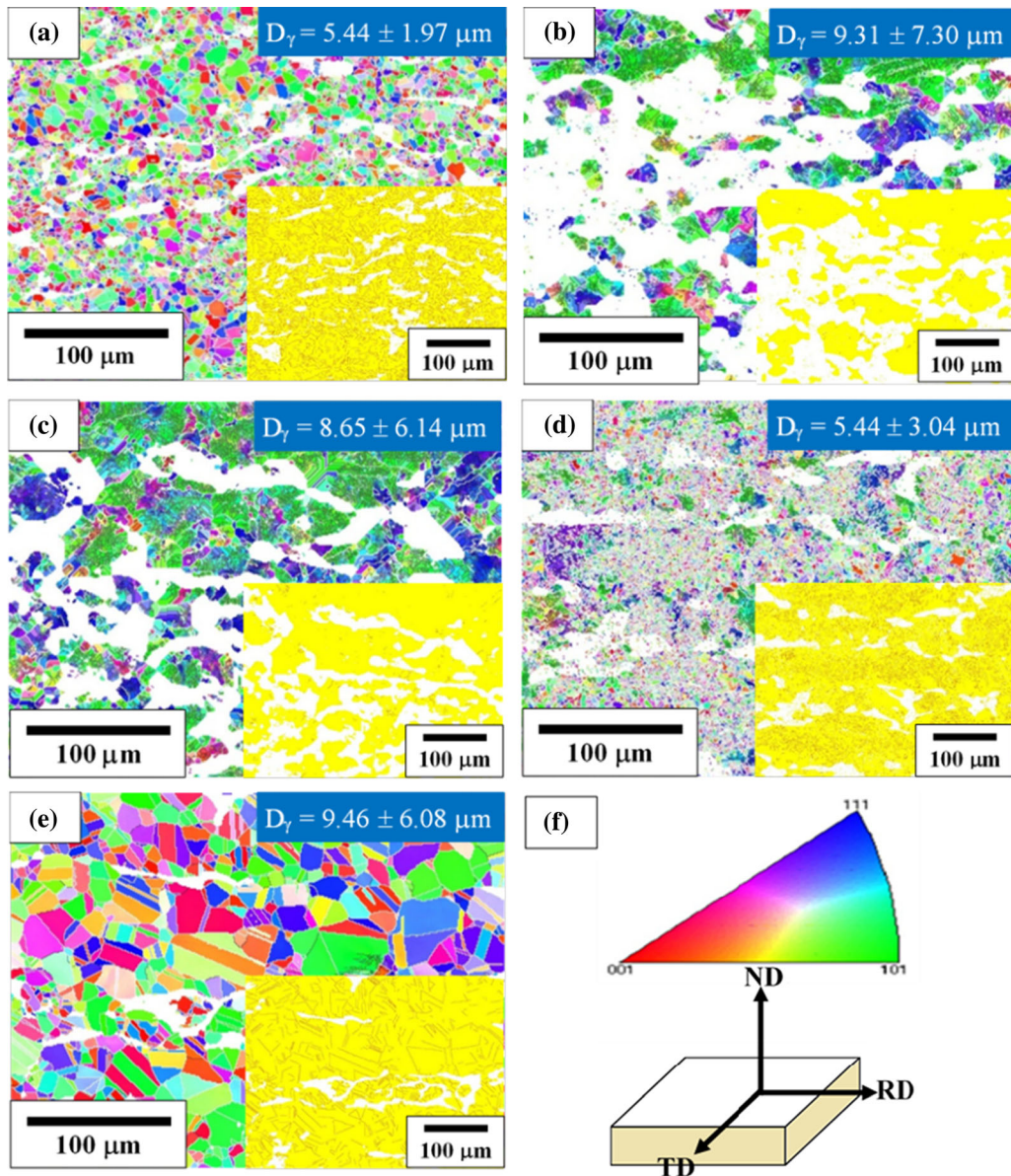


Fig. 4—ND-Inverse pole figure (IPF) maps of FCC austenite of (a) HRACST, (b) 50CD, and annealed (for 30 min) (c) at 500 °C (d) at 700 °C, (e) at 900 °C samples, (f) ND-IPF color legend. Inset diagrams in (a) to (e) are showing twin maps of the respective samples.  $D_\gamma$  indicates the average austenite grain size (Color figure online).

variation due to the presence of fine recrystallized grains along with the deformed coarse grains. At 500 °C, there is no signature of recrystallization and grain refinement. At higher annealing temperatures (700 °C to 900 °C), the initially deformed grains are replaced by the much finer recrystallized grains of sub-microns to a few microns in size (in Figures 4(d) and (e)), and thereby the original grain boundaries cannot be traced anymore.

Figures 5(a) through (e) represent the ND-IPF maps of the deformation-induced BCC ferrite (DIF) for HRACST, 50CD and annealed (at 500 °C, 700 °C and 900 °C for 30 minutes) samples. The DIF fraction is higher by ~ 16 to 17 pct in the 50CD sample than in the HRACST sample; see Figures 5(a) and (b). The amount of DIF remains the same at 500 °C for the 30-minute sample and reduces with the further increase in

annealing temperature (700 °C to 900 °C) due to the ferrite → austenite reverse transformation. The DIF grains are observed primarily along the austenite grain boundaries and become elongated upon cold deformation. The subsequent annealing leads to recovery of ferrite as it has a high stacking fault energy.<sup>[47]</sup> The recovery process continues up to 700 °C, which maintains a high frequency of the low-angle boundaries. Mohamadizadeh *et al.*<sup>[24]</sup> attributed the formation of low-angle boundaries to the dynamic recovery of the DIF. Dong *et al.*<sup>[48]</sup> reported that, due to various strain accumulations in ferrite, dislocation densities within the ferrite grains are low. These low dislocation densities and the rearrangement of dislocations develop the low-angle boundaries. At 900 °C, recrystallization dominates the microstructural restoration, which may even



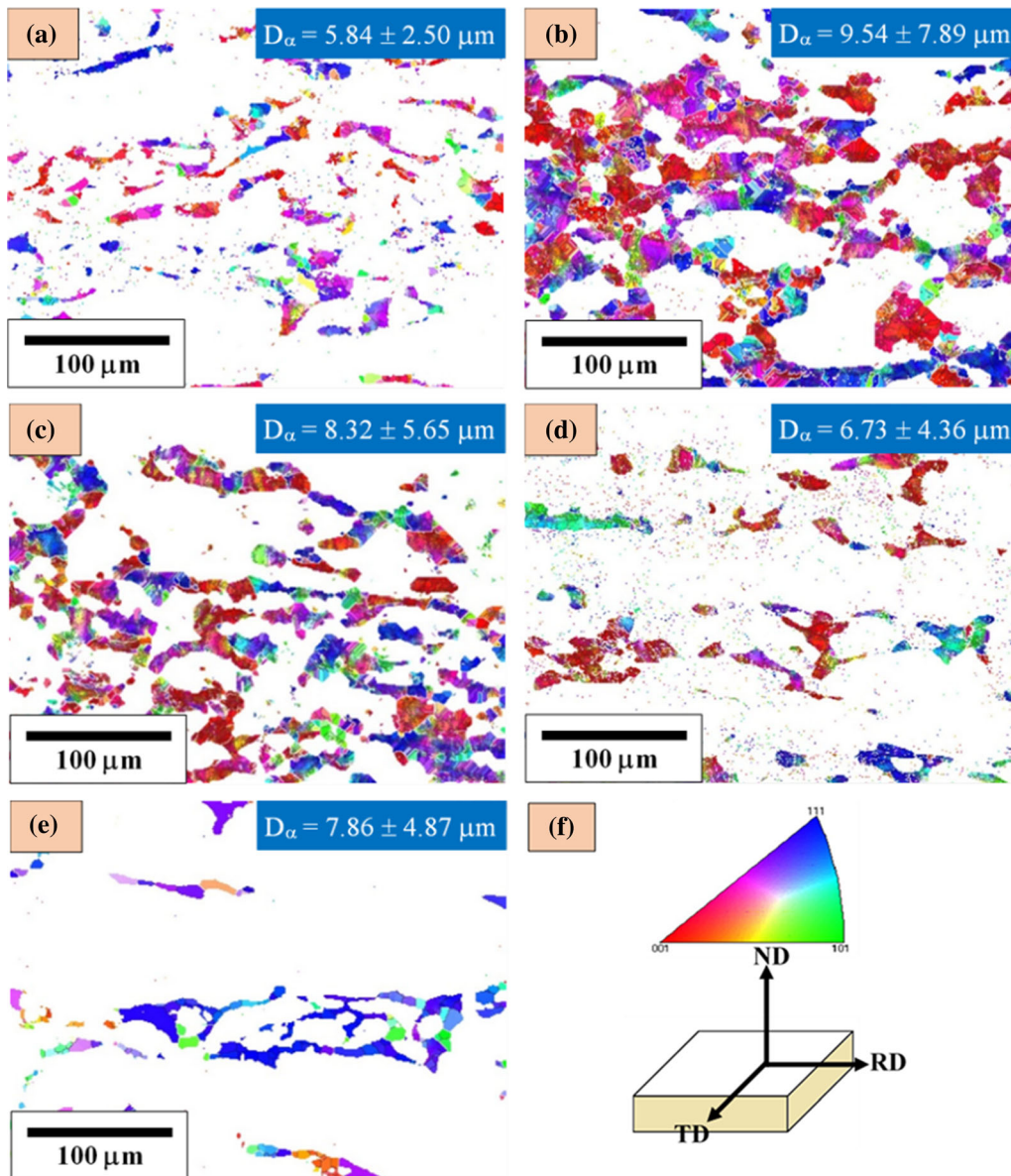


Fig. 5—ND-Inverse pole figure (IPF) maps of BCC ferrite (DIF) of (a) HRACST, (b) 50CD and annealed (for 30 min) (c) at 500 °C (d) at 700 °C, (e) at 900 °C samples and (f) ND-IPF color legend.  $D_z$  indicates the ferrite grain size (Color figure online).

be a continuous recrystallization process, aided by the pronounced ferrite recovery. Study of texture was taken up to identify the recrystallization mechanism.

Figure 6 displays the  $\phi_2 = 45$  deg sections of the orientation distribution function (ODF) of austenite for HRACST, 50CD and the annealed (at 500 °C, 700 °C and 900 °C for 30 minutes) samples. Annealing at 500 °C for 30 minutes shows Goss and Brass textures. Saleh *et al.*<sup>[27]</sup> reported that Cu texture component generally forms in high SFE materials, whereas low SFE leads to Brass type textures. During deformation, extensive twinning in the low-SFE steels can decrease the intensity of the copper component and increase the same for the Brass and Goss components.<sup>[49]</sup> However, the overall texture intensity of these components in the solution-treated sample is lower than those in the cold-deformed sample. The overall texture intensity further

decreases after annealing at 700 °C for 30 minutes, and Brass, Goss and S components deviate from their ideal locations and spread out. In this regard, it is important to note that a new orientation like transformed copper ( $\{255\}\langle 511 \rangle$ ) appears in Figure 6(d). Finally, the texture becomes more random in the 900 °C—30 minutes sample where the recrystallization of austenite strengthens the cube texture with some Goss texture (Figure 6(e)). The partially recrystallized samples (700 °C—30 minutes and 900 °C—30 minutes) primarily contain the same texture components as the cold-deformed sample but at a considerably lower intensity and substantial spreading of the orientations; see Figures 6(d) and (e). The annealing response, therefore, starts with the recovery-assisted nucleation of the new grains followed by their growth, which transforms the elongated grains into equiaxed grains at higher



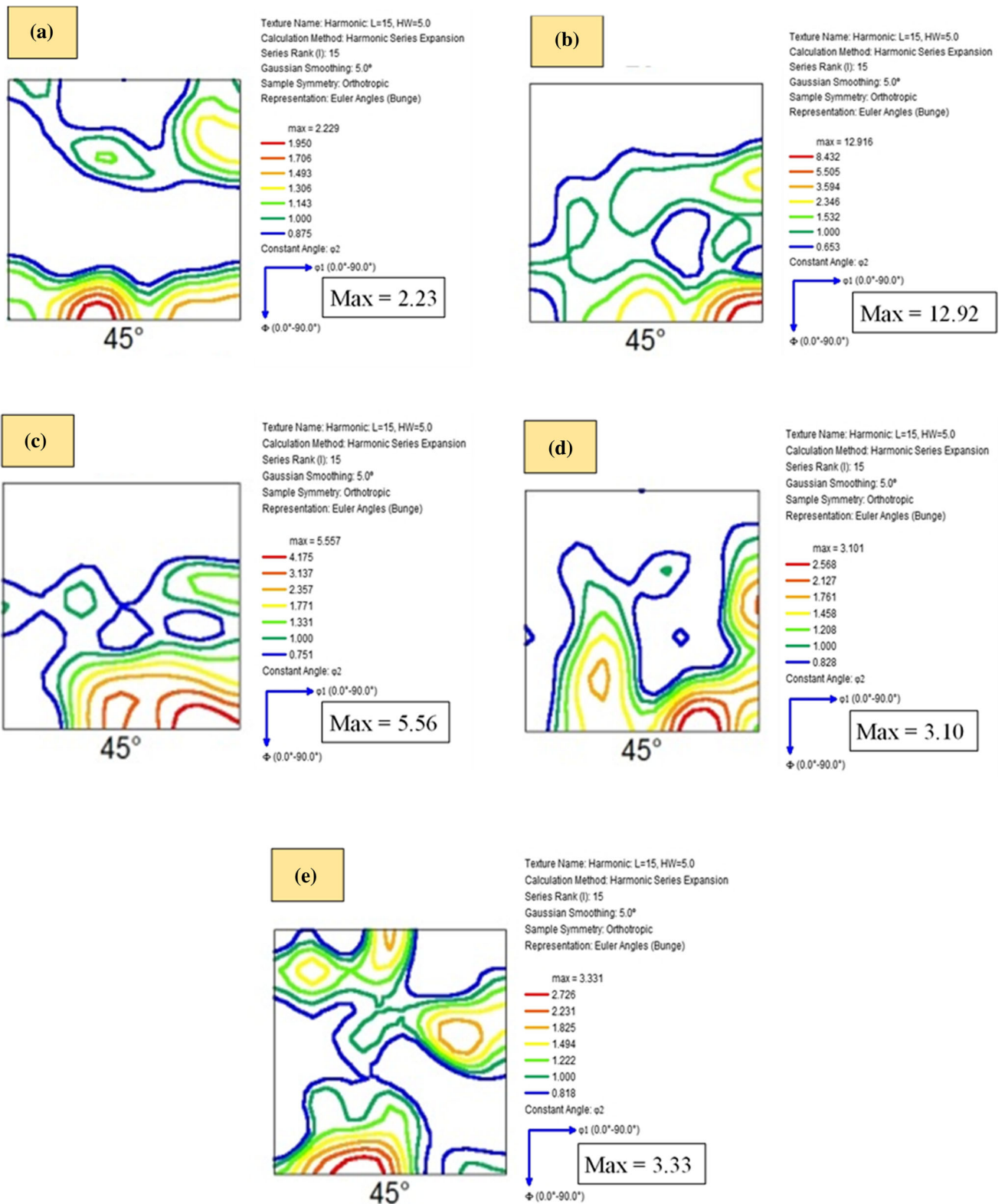


Fig. 6— $\Phi_2 = 45$  deg sections of the orientation distribution function (ODF) of austenite of (a) HRACST, (b) 50CD, and annealed (for 30 min) (c) at 500 °C (d) at 700 °C and (e) at 900 °C samples. The color legends (intensity) are given with the respective ODFs (Color figure online).

annealing temperature (900°C). Therefore, completely recrystallized samples do not reveal any strong texture component.

Figure 7 reveals the  $\phi_2 = 45$  deg sections of the ODF of deformation-induced ferrite for HRACST, 50CD and annealed (at 500 °C, 700 °C and 900 °C for 30 minutes)

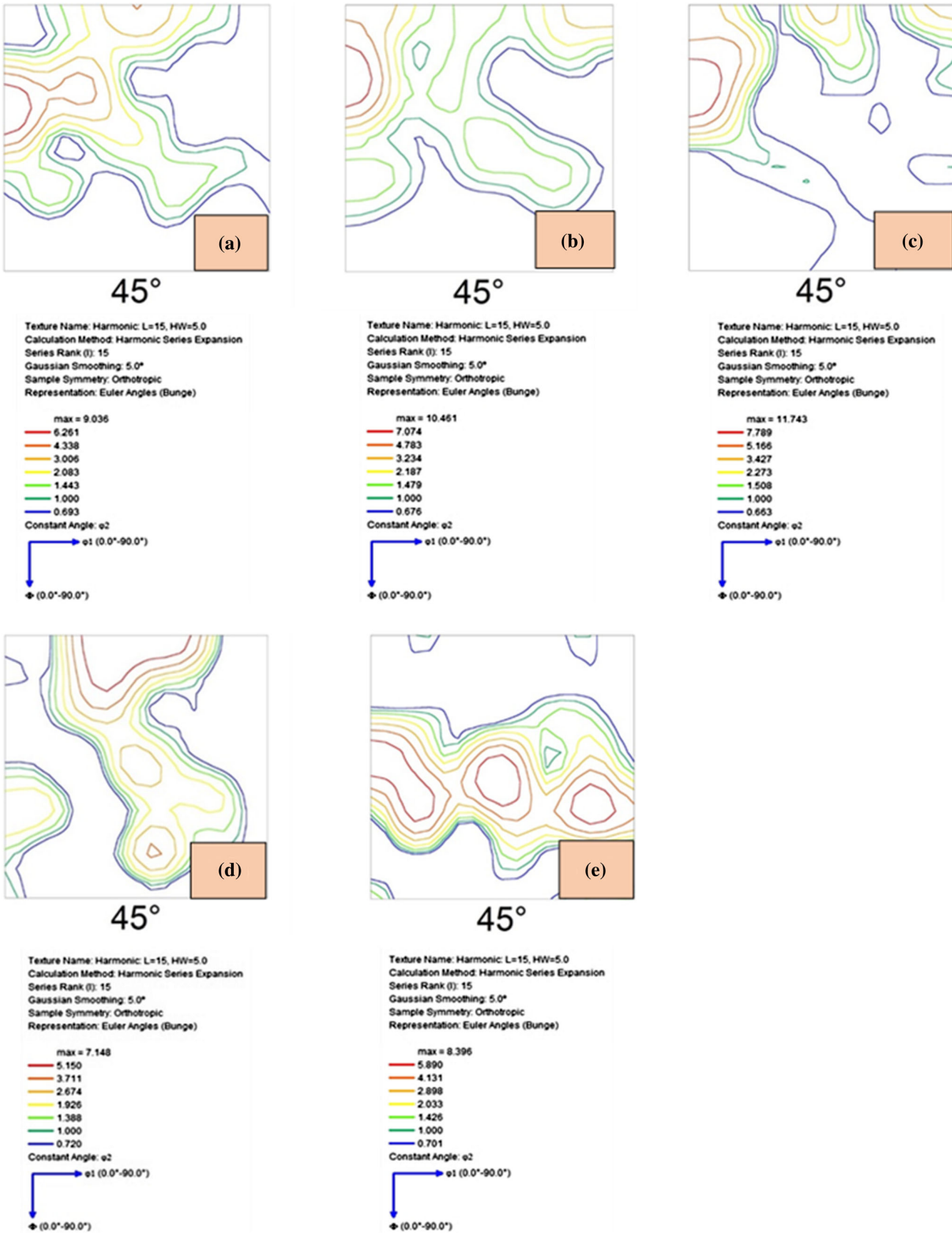


Fig. 7— $\Phi_2 = 45$  deg sections of the orientation distribution function (ODF) of deformation induced ferrite (DIF) of (a) HRACST, (b) 50CD and annealed (for 30 min) (c) at 500 °C (d) at 700 °C and (e) at 900 °C samples, the color legends (intensity) are given with the respective ODFs (Color figure online).



samples as obtained from the EBSD study. The color legends are given below the respective ODFs. Figure 7(a) shows a mixture of cube (RD// $\langle 001 \rangle$ ), alpha-fiber (RD// $\langle 110 \rangle$ ) and gamma-fiber (ND// $\langle 111 \rangle$ ) texture in HRACST. Typical deformation textures, such as alpha fiber and rotated cube, dominate in the 50CD sample. Alpha fiber, cube and rotated cube are also obtained in the 500 °C—30 minutes annealed sample. The texture changes to a mixture of cube (RD// $\langle 001 \rangle$ ) and gamma fiber (recrystallization texture) when the cold-deformed sample is annealed at 700 °C, whereas gamma fiber (ND// $\langle 111 \rangle$ ) dominates the texture in the 900 °C—30 minutes annealed sample. The strong gamma-fiber texture indicates that the conventional discontinuous recrystallization (and possibly not the continuous recrystallization) contributes to the restoration of the DIF grains (deformed after transformation) during high-temperature annealing of the dual-phase TWIP steel.

#### D. Mechanical Properties

Figure 8(a) shows the variation in hardness as a function of temperature for a fixed annealing time. The initial hardness of 175 HV in the HRACST sample increases to 400 HV in 50CD. The hardness decreases sharply with the increase in annealing time (from 5 minutes to 2 hours) at each annealing temperature. Figure 8(a) also indicates a gradual decrease in hardness with the increase in annealing temperature, and the lowest hardness obtained after annealing at 1000 °C for 2 hours (154 HV) is even lower than the hardness of the HRACST sample. Figures 8(b), (c) and 9(a), (b) show the engineering stress–strain curves of the samples annealed for 5 minutes, 30 minutes, and 1 hour and 2 hours, respectively. The curves for both the HRACST and 50CD samples are shown together for the sake of comparison. All the engineering stress–strain curves display continuous yielding behavior. Compared to the cold-deformed condition, the ductility (tensile strain) is significantly restored after annealing treatment, sacrificing yield and tensile strength, which is to be expected. The ultimate tensile strength (UTS) of the cold-rolled sample is 1202 MPa along with 20 pct total elongation. The maximum ductility of 82 pct is obtained after annealing at 1000 °C for 2 hours although the UTS decreases to 540 MPa. Some of the samples annealed at higher temperatures for longer durations show even better ductility but lower strength compared to the HRACST sample (655 MPa and 54 pct) because of the recrystallization and some amount of grain growth (up to 40 to 50  $\mu\text{m}$  in size) at the higher annealing temperatures for a prolonged duration. The sample annealed at 1000 °C for 5 minutes shows a similar stress–strain curve as the hot-rolled solution-treated sample (Figure 8(b)). However, the UTS and elongation are slightly higher because of the presence of thermally stable deformation twins and the recovered grain structure. The recovery happened even after the short duration of annealing (5 minutes) at a high temperature of 1000 °C ( $\gg$  500 °C).

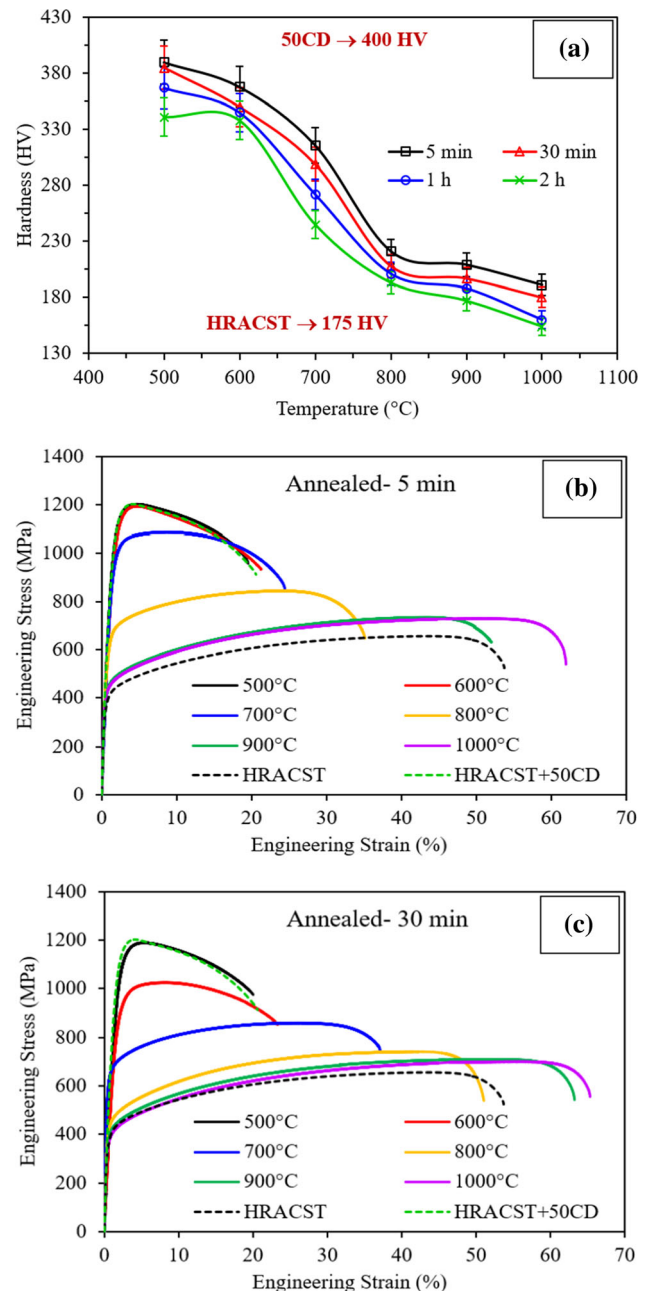


Fig. 8—(a) Variation in bulk hardness as the function of temperature. Engineering stress vs engineering strain curves of the samples annealed at 500 °C to 1000 °C for (b) 5 min and (c) 30 min.

Annealing at 700 °C for 30 minutes provides an excellent combination of strength and ductility with UTS of 859 MPa and total elongation of 37 pct, which can be attributed to the partially recrystallized austenite grain structure along with the ultrafine DIF grains. No considerable change can be noticed in the tensile properties after annealing the cold-rolled sample at 500 °C for up to 2 hours (Figure 9(b)). Some improvement in ductility (up to 27 and 30 pct) is observed after annealing at 600 °C for 1 to 2 hours. A significant restoration of ductility is obtained after annealing at 800 °C and 900 °C for 5 minutes to 2 hours. UTS of 745 MPa with 51 pct elongation is perceived in the 800

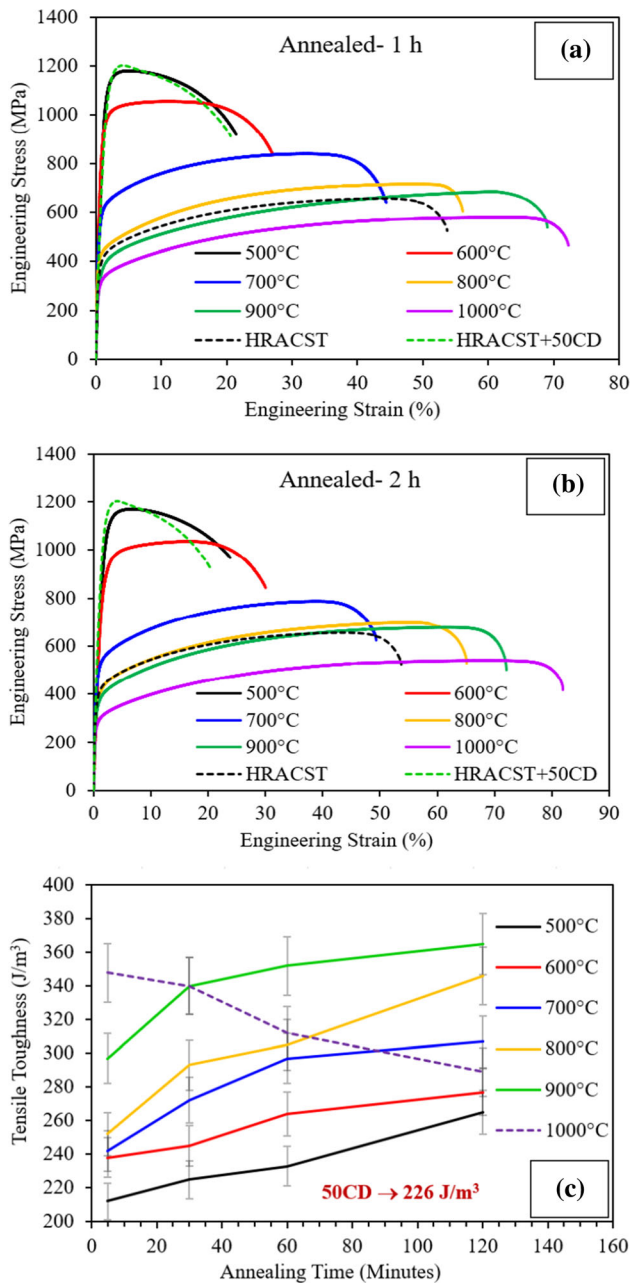


Fig. 9—Engineering stress vs engineering strain curves of the samples annealed at 500 °C to 1000 °C for (a) 1 h and (b) 2 h, and (c) variation in tensile toughness as the function of annealing time.

°C—30 minutes sample, whereas 708 MPa UTS with 63 pct ductility values is attained in the 900 °C—30 minutes sample. The annealing duration vs tensile toughness curve in Figure 9(c) indicates a continuous increase in tensile toughness (compared to the cold-rolled sample) with the increase in annealing temperature and time, except at 1000 °C (for 30 minutes to 2 hours) where the toughness decreases. At 1000 °C, the strength drastically decreases (possibly because of grain growth), affecting the tensile toughness. The maximum tensile toughness is obtained in the 900 °C—2 hours sample.

Figures 10(a) and (b) show the variation in recrystallization (pct) as a function of annealing temperature and

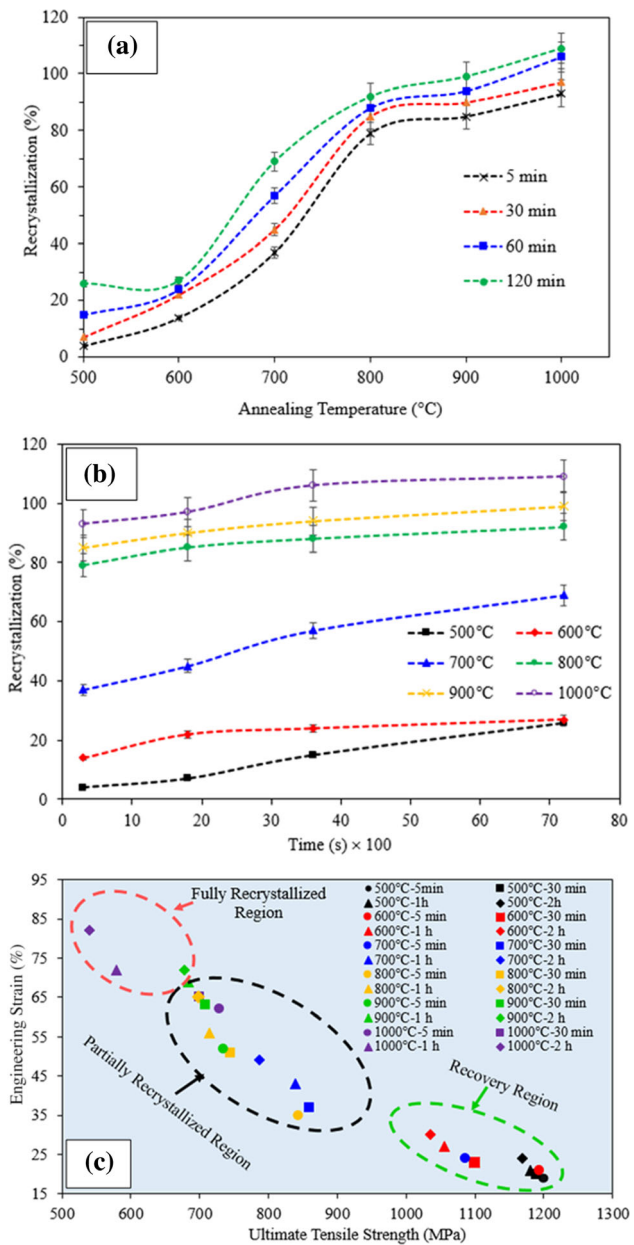


Fig. 10—Percent recrystallization as the function of (a) annealing temperature and (b) annealing time, (c) ultimate tensile strength (UTS) vs engineering strain plot represents three distinct regions, namely recovery, partially recrystallized and fully recrystallized region.

time, respectively. The recrystallization fraction increases significantly with the increase in annealing temperature, whereas the influence of annealing time is less pronounced. Annealing at 1000 °C for 1 to 2 hours completely recrystallized the microstructure, and the hardness decreased below that of the HRACST sample because of grain growth. At 900 °C, almost complete recrystallization (99 pct) was achieved after annealing for 2 hours. The UTS vs total elongation plot in Figure 10(c) for a wide range of annealing conditions primarily exhibits three distinct regions of microstructural restoration, viz. recovery, partial recrystallization and complete recrystallization (with grain growth).



Annealing at 500 °C and 600 °C for 5 minutes to 2 hours, and 700 °C for 5 minutes, resulted in recovery instead of recrystallization. Annealing at 700 °C and 800 °C for all durations and 900 °C up to 1 hour corresponds to the partial recrystallization region, where both deformed and recrystallized grains coexist. Annealing at 900 °C—2 hours, 1000 °C—1 hour and 1000 °C—2 hours yielded fully recrystallized microstructures. It can be inferred from Figure 10(c) that, upon annealing at lower temperatures (500 °C to 600 °C), ductility is restored to a limited extent with a marginal decrease in UTS because of recovery. The partially recrystallized region shows a reasonable amount of tensile strength (680–830 MPa) and ductility (40 to 65 pct) for the deformed samples annealed at 700 °C to 900 °C. Annealing at 1000 °C resulted in a substantial increase in ductility; however, the tensile strength was reduced significantly.

### E. Fractographic Features

Figure 11 displays SEM fractographs of the specimens tested for tensile strength. The HRACST sample shows ductile fracture characterized by fine and equiaxed dimples (Figure 11(a)). The 50CD fracture surface (Figure 11(b)) shows a brittle appearance comprising cleavage and quasi-cleavage (which can be the harder DIF regions) and microcracks (possibly formed at the interface of ferrite and austenite) elongated along the rolling direction (Figure 11(b)). Upon cold deformation of 50 pct, the equiaxed dimples decrease in size, and the coalescence of these dimples leads to microcrack initiation. The fractographic features did not change significantly after annealing at 500 °C for 1 hour (Figure 11(c)) compared to the 50CD sample. Therefore, the annihilation of the residual stress and deformation-induced defects improved the ductility without significant microstructural changes. The sample annealed at 700 °C (for 30 minutes to 1 hour duration) reveals fine dimples indicating a ductile fracture as shown in Figures 11(d) and (e). Figures 11(f) and (g) also show primarily ductile fracture after annealing at 900 °C (for 30 minutes to 1 hour).

The region of ductile fractures and the size of dimples have increased with annealing time at 900 °C. Annealing at 1000 °C for 2 hours led to a complete ductile fracture similar to the fracture surface of HRACST where the dimples are equiaxed and deep. Hence, it can be concluded that the brittle nature of fracture becomes the ductile mode of fracture with the increase in annealing temperature and time. Thus, the results of fractographic study substantiate the earlier discussion on the recrystallization fraction and tensile properties.

## IV. CORRELATION OF MICROSTRUCTURE, TEXTURE AND MECHANICAL PROPERTIES WITH ANNEALING BEHAVIOR

During the recovery annealing treatment, dislocation density ( $\rho$ ) can be expressed as<sup>[50]</sup>

$$\rho = \rho_m - \eta \ln(1 + \beta t) \quad [7]$$

where  $\rho_m$  is the dislocation density present in the cold-deformed specimen,  $\eta$  is the recovery constant, and  $\beta$  is the instantaneous recovery rate. Again,  $\beta$  can be expressed in terms of the Arrhenius equation as<sup>[50]</sup>

$$\beta = v \exp\left(-\frac{Q_{\text{rec}}}{KT}\right) \quad [8]$$

where  $v$  is a constant,  $Q_{\text{rec}}$  is the activation energy,  $K$  is the Boltzmann constant ( $8.6173303 \times 10^{-5}$  eV/K), and  $T$  is the absolute temperature (in K). If two sets of temperature and time ( $T$ ,  $t$ ) show similar hardness, then the samples are expected to have a similar dislocation density. Therefore, Eqs. [7] and [8] can be rewritten as<sup>[50]</sup>

$$\exp\left(-\frac{Q_{\text{rec}}}{KT}\right)t_1 = \exp\left(-\frac{Q_{\text{rec}}}{KT}\right)t_2 \quad [9]$$

From Eq. [9] the activation energy  $Q_{\text{rec}}$  can be expressed by<sup>[50]</sup>

$$Q_{\text{rec}} = \frac{KT_1 T_2 \ln(t_1 - t_2)}{(T_2 - T_1)} \quad [10]$$

Annealing at ‘500 °C for 1 hour’ and ‘600 °C for 5 minutes’ shows similar hardness, and the corresponding activation energy is 1.45 eV or 140 kJ/mol, which is close to the activation energy of dislocation of  $\gamma$ -Fe, *i.e.*, 1.65 eV or 159 kJ/mol.<sup>[50]</sup> According to a previous study,<sup>[51]</sup> the recovery of the deformed samples is controlled by diffusion through the dislocation cores. Similarly, the activation energy for another set of temperature and time such as ‘800 °C, 30 minutes’ and ‘900 °C, 5 minutes’ is 1.95 eV or 188 kJ/mol. This value lies in between the self-diffusion value (2.80 eV or 270 kJ/mol) and the core-diffusion value (1.65 eV or 159 kJ/mol) of  $\gamma$ -Fe, which implies that the recovery process reaches completion and recrystallization starts. On the other hand, the activation energy for ‘900 °C, 30 minutes’ and ‘1000 °C, 5 minutes’ is 2.31 eV or 222 kJ/mol. This value is very close to the self-diffusion of  $\gamma$ -Fe, which indicates that the recrystallization becomes the primary softening mechanism instead of recovery.

The microstructure, hardness and strength values are not altered significantly when the cold-deformed samples are annealed at 500 °C and 600 °C for different durations. However, at these temperatures, a certain increase in ductility indicates the structural recovery by the release of residual stress and annihilation and rearrangement of the dislocations. Twinning during deformation can hinder the subsequent recovery process by resisting the dislocation movement. The deformation texture remains even after the recovery annealing; however, the overall texture intensity decreases.

At 700 °C and 800 °C, partial recrystallization has taken place with very fine grains ( $<1 \mu\text{m}$ ) visible along with the coarser and deformed grains. The defect-free fine grains not only increase the strength following the

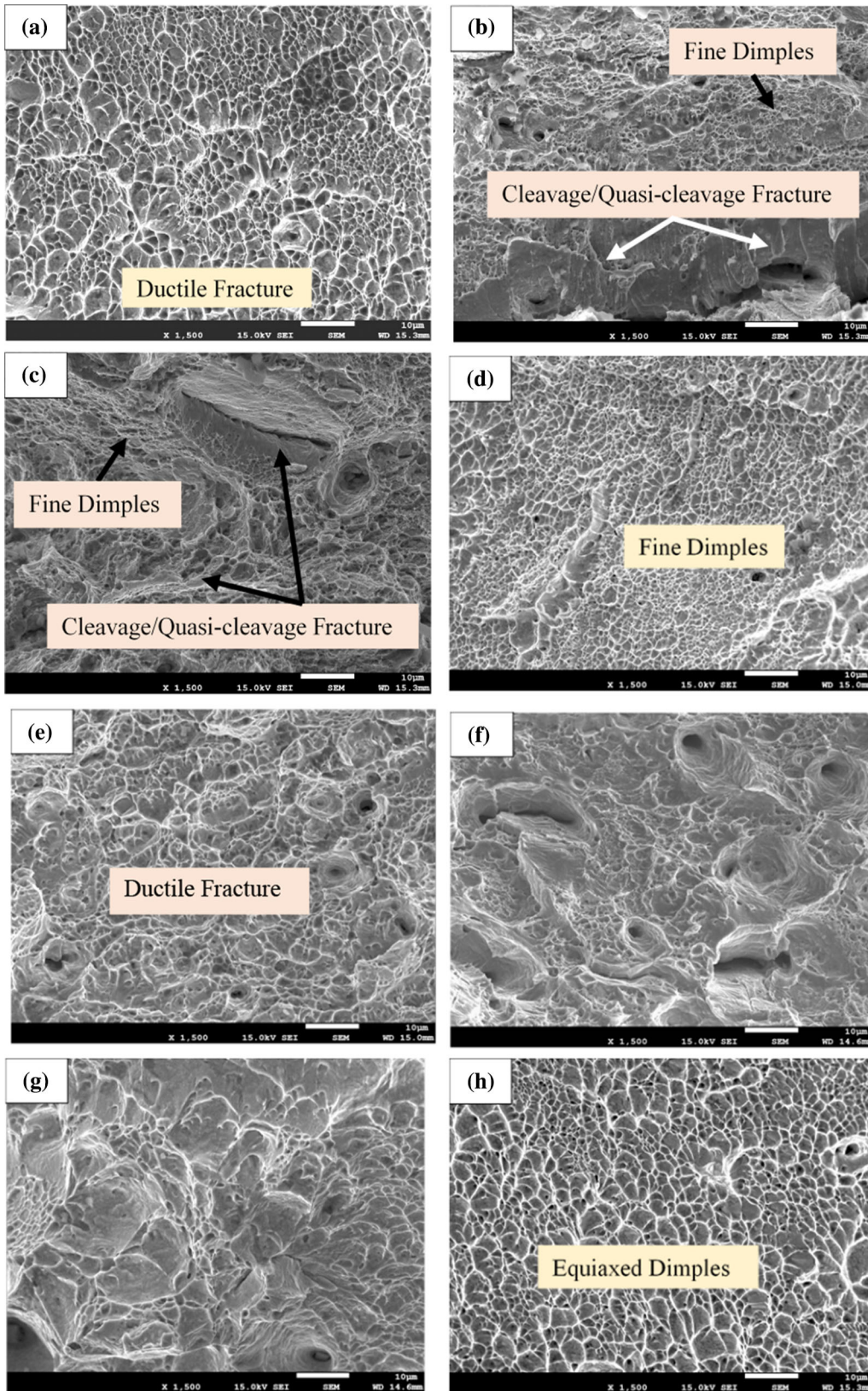


Fig. 11—SEM micrographs of tensile fracture surfaces of (a) HRACT, (b) 50CD and annealed, (c) 500 °C—1 h, (d) 700 °C—30 min, (e) 700 °C—1 h, (f) 900 °C—30 min, (g) 900 °C—1 h and (h) 1000 °C—2 h samples.



Hall–Petch relationship but also contribute to ductility and toughness. The deformed grains, as well as the ultrafine grains, maintain a higher strength level than that of the hot-rolled solution-treated samples (HRACST) as evident in Figures 8(b), (c) and 9(a), (b), whereas the defect-free recrystallized grains restore the ductility. As a result, the partially recrystallized samples showed the best combination of strength and ductility. The microstructure and EBSD study establish that the deformation twins do not act as the preferential nucleation sites for recrystallization. Rather, the grain boundaries and triple points provide the nucleation sites for recrystallization. It was reported earlier<sup>[52,53]</sup> that if cold-deformed grains remain in the annealed condition, the presence of deformation twins is to be expected. Annealing at 900 °C (for different durations) primarily results in recrystallization up to 99 pct in 2 hours. The partially recrystallized 700 °C—30 minutes and 900 °C—30 minutes samples do not reveal any strong recrystallization texture apart from the retention of some deformed grains with deformation texture (at a reduced intensity). The newly formed recrystallized austenite grains have a random orientation; therefore, the deformation texture becomes relatively weak in the partially recrystallized samples. After annealing at 900 °C for 1 to 2 hours and 1000 °C for 5 minutes and 30 minutes, the deformed grains are fully recrystallized increasing the ductility > 60 pct. Annealing at 1000 °C for 1 and 2 hours results in grain growth, which decreases the hardness and strength significantly even lower than the hot-rolled and solution-treated sample. The ductility on the other hand exceeds 80 pct.

The evolution of the texture of austenite in dual-phase TWIP steel is different from that in the single-phase austenitic steels—which is an interesting observation. Although Brass and Goss orientations are known to dominate the FCC deformation texture, the present study shows strong gamma-fiber texture in deformed austenite and a relatively weaker Goss and Brass orientations. This can be attributed to the influence of DIF. The transformation of the severely deformed austenite grains to DIF can reduce the intensity of Brass and Goss textures. On the other hand, the preferential deformation of austenite due to the constraint imposed by the harder DIF regions can also intensify the gamma-fiber in austenite. The DIF grains are also deformed by subsequent straining (during cold rolling), generating alpha-fiber and rotated cube deformation textures that finally turn into gamma fibers after recrystallization annealing.

## V. CONCLUSIONS

The following major conclusions can be derived based on the above experimental findings:

1. Optical microscopy, TEM and X-ray diffraction studies confirm that hot-rolled air-cooled and solution-treated and 50 pct cold-rolled samples show primarily austenitic structure along with deformation induced ferrite of 15 to 18 vol pct.

The formation of a superlattice structure inside DIF was confirmed by the TEM study.

2. Recrystallization initiates after annealing at 700 °C for 30 minutes and results in the formation of ultrafine grains (< 1 μm), which gradually increase in size with annealing temperature and time. These indicate that the recrystallization dominates instead of recovery. DIFs almost completely vanish after annealing at 900 °C by the reverse ferrite-to-austenite transformation.
3. The EBSD-IPF maps reveal that the DIFs are present primarily along the boundaries of cold-deformed and elongated austenite grains. The ferrite phase readily recovers because of its high stacking fault energy. At 900 °C, recrystallization takes place in deformed ferrite.
4. Annealing at 500 °C to 600 °C results in recovery, whereas partial recrystallization occurs upon annealing at 700 °C to 800 °C. Almost complete recrystallization is achieved upon annealing at 900 °C for 30 minutes to 2 hours and 1000 °C for 5 to 30 minutes. These results are also substantiated by the activation energy calculation through the Arrhenius equation.
5. An increase in the fraction of deformation-induced ferrite (DIF) after cold deformation can be correlated with dislocation-assisted diffusion through the short-circuiting paths (pipe diffusion) as well as the strain energy relaxation through an equal amount of reduction in the total Helmholtz free energy. A gradual decrease in hardness is observed with the increase in annealing temperature and time. The sample annealed at 1000 °C for 2 hours showed the lowest hardness (154 HV) as a result of grain growth.
6. Upon annealing, strength decreases (from 1202 to 540 MPa) and ductility significantly increases (from 20 to 82 pct). The optimum combination of strength and ductility is achieved in partially recrystallized samples annealed at 700 °C for 30 minutes (UTS: 859 MPa, tensile elongation: 37 pct) to 900 °C for 30 minutes (UTS: 708 MPa, tensile elongation: 63 pct). Fractography reveals fine dimples indicating the ductile mode of fracture with the increase in annealing temperature and time.

## REFERENCES

1. P. Lan and J. Zhang: *Metall. Mater. Trans. A*, 2018, vol. 49A, pp. 147–61.
2. P. Kürnsteiner, C. Commenda, E. Arenholz, L. Samek, D. Stifter, and H. Groiss: *Materialia*, 2018, vol. 1, pp. 70–77.
3. P.J. Gibbs, E. De Moor, M.J. Merwin, B. Clausen, J.G. Speer, and D.K. Matlock: *Metall. Mater. Trans. A*, 2011, vol. 42A, pp. 3691–3702.
4. G.M. de Bellefon, M.N. Gussev, A.D. Stoica, J.C. van Duysen, and K. Sridharan: *Scripta Mater.*, 2018, vol. 157, pp. 162–66.
5. O. Grässel, L. Krüger, G. Frommeyer, and L.W. Meyer: *Int. J. Plast.*, 2000, vol. 16, pp. 1391–1409.

6. M. Bobby Kannan, R.K. Singh Raman, and S. Khoddam: *Corr. Sci.*, 2008, vol. 50, pp. 2879–84.
7. Y.S. Chun, K.-T. Park, and C.S. Lee: *Scripta Mater.*, 2012, vol. 66, pp. 960–65.
8. K. Jeong, J.-E. Jin, Y.-S. Jung, S. Kang, and Y.-K. Lee: *Acta Mater.*, 2013, vol. 61, pp. 3399–3410.
9. E. Kozeschnik and H.K.D.H. Bhadeshia: *Mater. Sci. Technol.*, 2008, vol. 24, pp. 343–47.
10. D.T. Pierce, D.R. Coughlin, K.D. Clarke, E. De Moor, J. Poplawsky, D.L. Williamson, B. Mazumder, J.G. Speer, A. Hood, and A.J. Clarke: *Acta Mater.*, 2018, vol. 151, pp. 454–69.
11. D.T. Pierce, D.R. Coughlin, D.L. Williamson, J. Kähkönen, A.J. Clarke, K.D. Clarke, J.G. Speer, and E. De Moor: *Scripta Mater.*, 2016, vol. 121, pp. 5–9.
12. L. Fu, M. Shan, D. Zhang, H. Wang, W. Wang, and A. Shan: *Metall. Mater. Trans. A*, 2017, vol. 48A, pp. 2179–92.
13. O. Bouaziz and N. Guelton: *Mater. Sci. Eng. A*, 2001, vols. 319–321, pp. 246–49.
14. G. Dini, A. Najafizadeh, R. Ueji, and S.M. Monir-Vaghef: *Mater. Des.*, 2010, vol. 31, pp. 3395–3402.
15. E. Bagherpour, M. Reihanian, and R. Ebrahimi: *Mater. Des.*, 2012, vol. 36, pp. 391–95.
16. C.Y. Sun, N. Guo, M.W. Fu, and S.W. Wang: *Int. J. Plast.*, 2016, vol. 76, pp. 186–212.
17. Z.C. Luo and M.X. Huang: *Scripta Mater.*, 2018, vol. 142, pp. 28–31.
18. N.K. Tewary, S.K. Ghosh, S. Chatterjee, and A. Ghosh: *Mater. Sci. Eng. A*, 2018, vol. 733, pp. 43–58.
19. X. Li, L. Chen, Y. Zhao, and R.D.K. Misra: *Mater. Des.*, 2018, vol. 142, pp. 190–202.
20. D.B. Santos, A. Saleh, A.A. Gazder, A. Carman, D.M. Duarte, É.A.S. Ribeiro, B.M. Gonzalez, and E.V. Pereloma: *Mater. Sci. Eng. A*, 2011, vol. 528, pp. 3545–55.
21. D.P. Escobar, S.S.F. de Dafé, and D.B. Santos: *J. Mater. Res. Technol.*, 2015, vol. 4, pp. 162–70.
22. Z. Yanushkevich, A. Belyakov, R. Kaibyshev, C. Haase, and D.A. Molodov: *Mater. Charact.*, 2016, vol. 112, pp. 180–87.
23. J. Zhang, D. Raabe, and C.C. Tasan: *Acta Mater.*, 2017, vol. 141, pp. 374–87.
24. A. Mohamadizadeh, A. Zarei-Hanzaki, A. Kisko, and D. Porter: *Mater. Des.*, 2016, vol. 92, pp. 322–29.
25. B. Bhattacharya, R.K. Ray, and T. Leffers: *Metall. Mater. Trans. A*, 2015, vol. 46A, pp. 5296–5307.
26. Y.F. Shen, C.H. Qiu, L. Wang, X. Sun, X.M. Zhao, and L. Zuo: *Mater. Sci. Eng. A*, 2013, vol. 561, pp. 329–37.
27. A.A. Saleh, E.V. Pereloma, and A.A. Gazder: *Mater. Sci. Eng. A*, 2011, vol. 528, pp. 4537–49.
28. Y. Lü, D.A. Molodov, and G. Gottstein: *Acta Mater.*, 2011, vol. 59, pp. 3229–43.
29. N.K. Tewary, S.K. Ghosh, S. Bera, D. Chakrabarti, and S. Chatterjee: *Mater. Sci. Eng. A*, 2014, vol. 615, pp. 405–15.
30. V. Torabinejad, A. Zarei-Hanzaki, M. Sabet, and H.R. Abedi: *Mater. Des.*, 2011, vol. 32, pp. 2345–49.
31. V. Torabinejad, A. Zarei-Hanzaki, S. Moemeni, and A. Imandoust: *Mater. Des.*, 2011, vol. 32, pp. 5015–21.
32. A. Imandoust, A. Zarei-Hanzaki, M. Sabet, and H.R. Abedi: *Mater. Des.*, 2012, vol. 40, pp. 556–61.
33. M.H. Razmpoosh, A. Zarei-Hanzaki, N. Haghdad, J.-H. Cho, W.J. Kim, and S. Heshmati-Manesh: *Mater. Sci. Eng. A*, 2015, vol. 638, pp. 5–14.
34. A. Imandoust, A. Zarei-Hanzaki, S. Heshmati-Manesh, S. Moemeni, and P. Changizian: *Mater. Des.*, 2014, vol. 53, pp. 99–105.
35. I.N. Levine: *Physical Chemistry*, 6th ed., McGraw-Hill Higher Education, New York, 2008, p. 109.
36. T. Matsushita and K. Mukai: *The First Law of Thermodynamics: Chemical Thermodynamics in Materials Science, Chapter 7*, Springer, Singapore, 2018, pp. 17–22.
37. C. Zheng, N. Xiao, L. Hao, D. Li, and Y. Li: *Acta Mater.*, 2009, vol. 57, pp. 2956–68.
38. N. Xiao, M. Tong, Y. Lan, D. Li, and Y. Li: *Acta Mater.*, 2006, vol. 54, pp. 1265–78.
39. X. Sauvage and Y. Ivanisenko: *J. Mater. Sci.*, 2007, vol. 42, pp. 1615–21.
40. L. Zhao, N. Park, Y. Tian, A. Shibata, and N. Tsuji: *Mater. Res. Lett.*, 2018, vol. 6, pp. 641–47.
41. N.K. Tewary, S.K. Ghosh, R. Saha, and S. Chatterjee: *Philos. Mag.*, 2019, vol. 99, pp. 2487–2516.
42. L. Liu, C. Li, Y. Yang, Z. Luo, C. Song, and Q. Zhai: *Mater. Sci. Eng. A*, 2017, vol. 679, pp. 282–91.
43. B. Bhattacharya, A.S. Sharma, S.S. Hazra, and R.K. Ray: *Metall. Mater. Trans. A*, 2009, vol. 40A, pp. 1190–1202.
44. A. Imandoust, A. Zarei-Hanzaki, K.-L. Ou, and C.-H. Yu: *J. Mater. Eng. Perform.*, 2015, vol. 24, pp. 2085–90.
45. E. Welsch, D. Ponge, S.M. Hafez Haghghat, S. Sandlöbes, P. Choi, M. Herbig, S. Zaefferer, and D. Raabe: *Acta Mater.*, 2016, vol. 116, pp. 188–99.
46. D.B. Williams and C.B. Carter: *Transmission Electron Microscopy*, 2nd ed., Springer, Boston, 2009, pp. 262–65.
47. W. Reick, M. Pohl, and A.F. Padilha: *Steel Res. Int.*, 1996, vol. 67, pp. 253–56.
48. H. Dong and X. Sun: *Curr. Opin. Solid State Mater. Sci.*, 2005, vol. 9, pp. 269–76.
49. L. Bracke, K. Verbeken, L. Kestens, and J. Penning: *Acta Mater.*, 2009, vol. 57, pp. 1512–24.
50. G.W. Yuan and M.X. Huang: *Prog. Nat. Sci.*, 2014, vol. 24, pp. 50–55.
51. R. Song, D. Ponge, D. Raabe, and R. Kaspar: *Acta Mater.*, 2005, vol. 53, pp. 845–58.
52. F. Berrenberg, C. Haase, L.A. Barrales-Mora, and D.A. Molodov: *Mater. Sci. Eng. A*, 2017, vol. 681, pp. 56–64.
53. A. Hamada and J. Kömi: *Mater. Sci. Eng. A*, 2018, vol. 718, pp. 301–04.

**Publisher's Note** Springer Nature remains neutral with regard to jurisdictional claims in published maps and institutional affiliations.